



Article

Transition Metal Chelation Effect in MOF-253 Materials: Guest Molecule Adsorption Dynamics and Proposed Formic Acid Synthesis Investigated by Atomistic Simulations

Meng-Chi Hsieh ¹, Wei-Lun Liang ¹, Chun-Chih Chang ^{2,*} and Ming-Kang Tsai ^{1,3,*}

¹ Intelligent Computing for Sustainable Development Research Center, Department of Chemistry, National Taiwan Normal University, Taipei 11677, Taiwan

² Department of Chemical and Materials Engineering, Chinese Culture University, Taipei 11114, Taiwan

³ Department of Chemistry, Fu-Jen Catholic University, New Taipei City 24205, Taiwan

* Correspondence: zjz8@ulive.pccu.edu.tw (C.-C.C.); mktsai@ntnu.edu.tw (M.-K.T.)

Abstract: The dynamic characterization of guest molecules in the metal–organic frameworks (MOFs) can always provide the insightful and inspiring information to facilitate the synthetic design of MOF materials from the bottom-up design of perspective. Herein, we present a series of atomistic molecular dynamics simulation for investigating the bipyridine dicarboxylate (bpydc) linker rotation effect on guest molecule adsorption with and without considering the transition metal (TM) chelation in MOF-253 materials. The simulated PXRD patterns of the various linker orientations present the challenge of distinguishing these structural varieties by the conventional crystalline spectroscopic measurements. The observed short inter-TM stable structure may subsequently lead to the formation of a binuclear TM catalytic site, and a proposed formic acid generation mechanism from CO₂ and H₂ is derived based upon the density functional theory calculations for the application of CO₂ reduction.

Keywords: metal–organic framework; CO₂ reduction; atomistic simulation



Citation: Hsieh, M.-C.; Liang, W.-L.; Chang, C.-C.; Tsai, M.-K. Transition Metal Chelation Effect in MOF-253 Materials: Guest Molecule Adsorption Dynamics and Proposed Formic Acid Synthesis Investigated by Atomistic Simulations. *Molecules* **2024**, *29*, 3211. <https://doi.org/10.3390/molecules29133211>

Academic Editor: Rita Prosimiti

Received: 17 May 2024

Revised: 29 June 2024

Accepted: 3 July 2024

Published: 5 July 2024



Copyright: © 2024 by the authors. Licensee MDPI, Basel, Switzerland. This article is an open access article distributed under the terms and conditions of the Creative Commons Attribution (CC BY) license (<https://creativecommons.org/licenses/by/4.0/>).

1. Introduction

Synthesized by the self-assembly of metal secondary building units (SBUs) and organic compounds, metal–organic frameworks (MOFs) have been increasingly studied for application over decades [1]. Attributing to the nature of MOFs, for example, their high surface area, versatility, being easily tunable, etc., MOFs could provide a suitable template for catalysts by using the bared SBUs directly [2,3] or using the cooperated metal nanoparticles or functional groups after modification [4–6]. Among these modifications, introducing the concept of metal complexes into the MOFs brings the benefit from both homogeneous and heterogeneous catalysts. It is also possible to make use of the experience accumulated over the past century [7].

Compared to other heterogeneous catalysts binding with metal complexes, MOFs are suited for studying the mechanism by the regular arrangement of building units. In the late 1990s, metal–ligand complexes were introduced as linkers by pre-synthesis. Later, Seo et al. included the racemic Ru(2,2'-bipy)₃²⁺ into L-POST-1 by post-synthesis modification (PSM) [8]. Lin and coworkers utilized the M[4,4'-(HO₂C)₂-bpy]₂bpy²⁺ with Zn to synthesize the M-doped MOF and further showed the capability of photo-harvest and energy transfer [9]. They also introduced the Ir, Re, and Ru complex to UIO-67 by the mix-and-match synthetic strategy with the pre-synthesized linker [10]. Owing to the vacant chelating sites that provide the possibility of post-synthetic metalation, the linkers containing nitrogen atoms have gained increasing attention in the last decade [11]. Because of the wide application of 2,2'-bipyridine (bpy) due to the photo-related properties of its metal complexes, it is one of the most notable bidentate chelators [12]. In 2010, Bloch et al. replaced the biphenyl dicarboxylate in DUT-5 with 2,2'-bipyridine-5,5'-dicarboxylic acid

(bpydc) as the linker to the synthesis of the aluminum-based MOF-253. The adsorption of flue gas showed increasing selectivity to CO₂ over N₂ after the PSM strategy introduced Cu(BF₄)₂ to MOF-253. The PdCl₂ was also introduced to MOF-253. Both PdCl₂ and Cu(BF₄)₂ insertion maintained the framework, being observed by the powder X-ray diffraction (PXRD) spectrum [13]. Then, a similar idea was adopted by the post-synthetic exchange (PSE) of the linker in UIO-67 to create UIO-67-bpydc [14]. There are some other MOFs with open bpydc linkers that were designed to achieve specific capabilities [15,16].

Since MOF-253 is a two-dimensional structure, the tube-like channel could provide a clear vision of how the guest molecule approaches the structure. Furthermore, MOF-253 has been investigated for CO₂ restoration [17] and CO₂ reduction reaction (CO₂RR) [18–20]. In a previous study, the reaction pathway of formic acid formation by CO₂RR with MOF-253 and H₂ was depicted [21]. It also elaborated on how the idea of homogeneous catalytic mechanisms could inspire the reaction in framework structures and how the steric effects of MOFs could affect these reactions. The computational results provided the thermodynamical details of the reaction mechanism, but the dynamical interplay between reactant and metal center remains unsettled. Additionally, the linker rotation is one of the factors that affect the collision between molecules in MOFs, but it was not well explored [22].

The linker rotation can bring new structural diversity and subsequently results new transition metal chelation effect. This structural diversity could consequently introduce various steric hindrance or electronic properties [23]. The rotation originates from the flexibility of organic components, especially for linkers with rigid parts hanging by single bonds. All of the topology [24], the guest molecule [25], and the electronic distribution [26] decide the feasibility of the rotation. 2,2'-bipyridine-5,5'-dicarboxylate, as linkers, confers two rotation portions (Figure 1). Each of them has a C_{py}-C_{carbonyl} single bond to connect the terminal carboxyl group, which is fixed on the node, and they have C_{py}-C_{py} single bonds to connect with one another. Wu et al. have demonstrated the rotation of bpydc from *cis*-NN (N and N' in the same direction of the linker) to stable *trans*-NN (N and N' in a different direction of linker) with 0.42 eV activation energy by quantum computational methods [17]. They concluded that the synthetic processes under room temperature could promote the transformation between the isomers and lead to different lattice parameters.

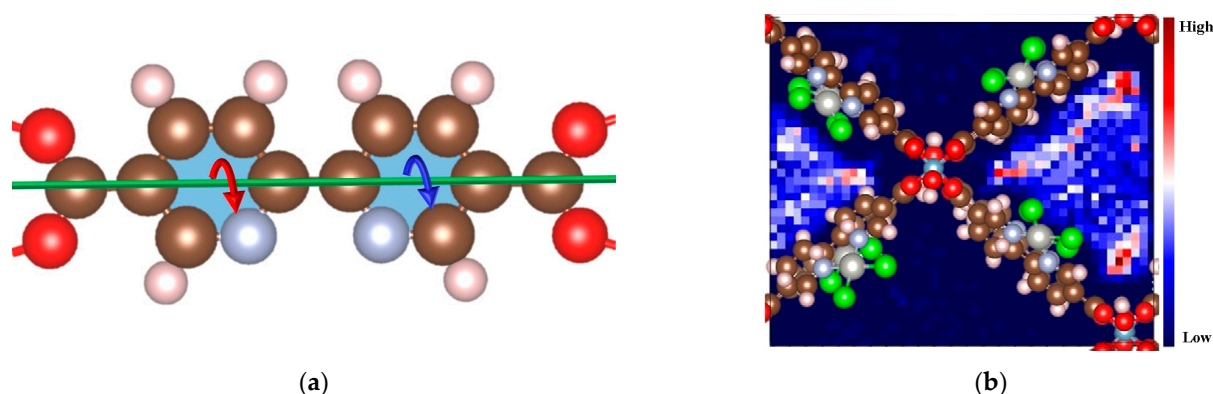


Figure 1. The schematic representations of (a) bpydc moiety rotation and (b) gas diffusion in MOF-253. The brown, red, pink, indigo, gray, and green denote carbon, oxygen, hydrogen, nitrogen, palladium, and chlorine atoms, respectively. The red and blue curved arrows (left) suggest that the two bpydc moieties' rotations do not necessarily correlate. The color blocks (right) denote the probability of guest molecule diffusion projected in a two-dimensional perspective.

In this study, the investigation focuses on the contribution of the linker's rotation and the guest molecule's distribution in MOF-253 by classical mechanics, molecular dynamics (MD), and density functional theory (DFT) simulation. The simulated PXRD spectra also give insight into the metal-incorporated MOF-253. Herein, an example of the transition metal (TM) dimer formed by the rotation of linkers as the catalyst is discussed. Predictably, the dimer might shortly give a synergetic effect with a good design of the incorporated complexes.

2. Results and Discussion

2.1. The Dynamics Phenomenon of Linker in MOF-253

In order to understand the underlying thermodynamical difference described at two different theory levels (FF vs. DFT), the rotation barrier along the C1-C2-C3-C4 dihedral angle of the linker with an orientation from trans-NN to cis-NN was calculated using the unit cell model shown in Figure S1. The calculated DFT barrier is approximately predicted at 10.7 kcal/mol in comparison with the corresponding case at 18.4 kcal/mol using FF calculation. The lower energy barrier predicted by DFT appears to indicate that linker rotation could be observed at a $T < 700$ K condition if the computationally expensive DFT-MD simulations are carried out. However, the FF-MD simulations at the $T > 700$ K condition can still provide a qualitative thermal-dependent description for the dynamic interplay of guest molecules and linker of MOF materials.

The FF-MD simulations started with using the supercells of L, L₆, LPdCl₂, and (LPdCl₂)₆ without the presence of gas molecules. The initial linker orientation adopted cis-NN orientation for all types of supercells (Figure S1a,b). All supercells were pre-equilibrated for 0.5 ns, and Table S1 summarized the thermodynamics at different temperatures during the production runs. As shown by the standard deviation of the average energy and temperature, it is reasonable to interpret that these supercells were under the equilibrium condition using the frozen lattice-constant models. Table S2 summarized the histograms of the dihedral angle of C1-C2-C3-N4 based upon the results of L and L₆ supercells. A linker orientation transition was observed for cis-NN (180 degree) to trans-NN (0 degree) transformation in the case of $T > 700$ K, and is schematically demonstrated in Figure S2. For the cases at $T \leq 700$ K, the bpy moiety could still be well twisted as depicted by the distribution of the C1-C2-C3-N4 angle in Table S2.

The dihedral angle of O5-C6-C7-C8 describes the distortion between the pyridine ring and the carboxylate anchor. For all types of supercells (with and without metal chelation), the pyridine ring can flip in respect to the non-mobile carboxylate anchor at $T > 700$ K as summarized in Table S3. With the inclusion of PdCl₂ chelation and the LPdCl₂ and (LPdCl₂)₆ supercells, the dihedral angles of O5-C6-C7-C8 at the resting condition were found to be well twisted to around 150 degrees, suggesting the presence of substantial steric hindrance introduced by the metal chelation. If the O5-C6-C7-C8 flips to zero degrees, a face-to-face PdCl₂ dimer structure would form, consequently providing a short Pd-Pd distance structure at about 3.48 Å as schematically shown in Figure S3.

As implied by the aforementioned molecular dynamics simulations, the thermal energy at the finite temperature condition could populate the various linker orientations with or without the metal chelation. This structural entropic effect may influence the guest molecules' adsorption as well as the design strategy of the post-synthesis modification of MOF-253 materials.

2.2. The Adsorption of the Guest Molecules in MOF-253

The adsorption behavior of guest molecules, including CO₂, N₂, and H₂, was also investigated using the molecular dynamics simulations. The comparison of the optimized geometries of these molecules using FF and DFT theory levels is listed in Table S4. Tables S5–S7 present the recorded statistics for the CO₂ in the vacuum, MOF-253, and PdCl₂-chelated MOF-253 models, respectively, at various temperatures. Tables S8 and S9 report the counterparts of N₂ and H₂ in the vacuum, respectively. The adsorption histogram of CO₂, H₂, and N₂ in L and LPdCl₂ models are schematically presented by the heat maps in Figure S5, in which each color pixel (block) represents the events of guest molecules appearing in the $0.5 \times b\text{-axis} \times 0.5 \text{ \AA}^3$ cuboid, and are projected on the two-dimensional map of ac-plane. The color code of each pixel denotes the event count based upon the recorded snapshots during the production run. Figures S6 and S7 provide the similar results of projecting on the ab-plane and bc-plane, respectively, using the exact same procedure as described above. All guest molecules were initially placed in one pore—two separated pores are present in the current simulation supercell. The distribution of color pixels for

CO₂ appears to be most localized, sequentially followed by N₂ and H₂, as observed in the L and LPdCl₂ series of simulations. N₂ and H₂ appear to be more mobile based upon their notable color pixels recorded near the central region of the pores. The localization adsorption of CO₂ in respect to N₂ simulated under 300 K consistently aligns with the previous experimental observation in MOF-253 and MOF-253-Pd materials, as CO₂ is a stronger adsorbate than N₂ [13].

All of the guest molecules have shown a preferential adsorption at nodes situated at the linker moieties with or without the PdCl₂ chelation. The higher probability of node adsorption may emphasize the importance of node engineering development to introduce the catalytic capability at this region. However, such a design approach could result in more complex synthetic challenges in comparison with the straightforward post-synthesis transition metal chelation. The mobile guest molecule diffusion could still result in substantial adsorption events at the PdCl₂ site if the pressure of the guest molecule is well controlled.

Figure 2 provides the statistics of the observed dynamics of guest molecules (H₂ and CO₂) penetrating the MOF framework to enter the neighboring pore. One hydrogen molecule was initially residing at one pore and was physically blocked by the linker orientation of the minimum energy structure. Without the PdCl₂ chelation, this small guest molecule appears to localize at the initial pore at simulations of 500 K and 700 K, until reaching the temperature at 1000 K to penetrate between the neighboring pores (see the comparison of Figure 2a–c). Darker pixels were generally observed near the linker surface region in comparison with the center region of the pores, suggesting the presence of the intermolecular “friction” that resulted from the interactions of the MOF-253 framework. With the incorporation of PdCl₂ chelation, H₂ appears to significantly populate at both pores at 500 K and 1000 K (see Figure 2d,e). The steric hindrance introduced by PdCl₂ chelation can twist the neighboring linkers, as schematically shown in Figure S1b—the presence of PdCl₂ moiety can break the coplanar nature of bipyridine. This consequently facilitates the PdCl₂-coordinated linker rotation as being notably observed at 500 K.

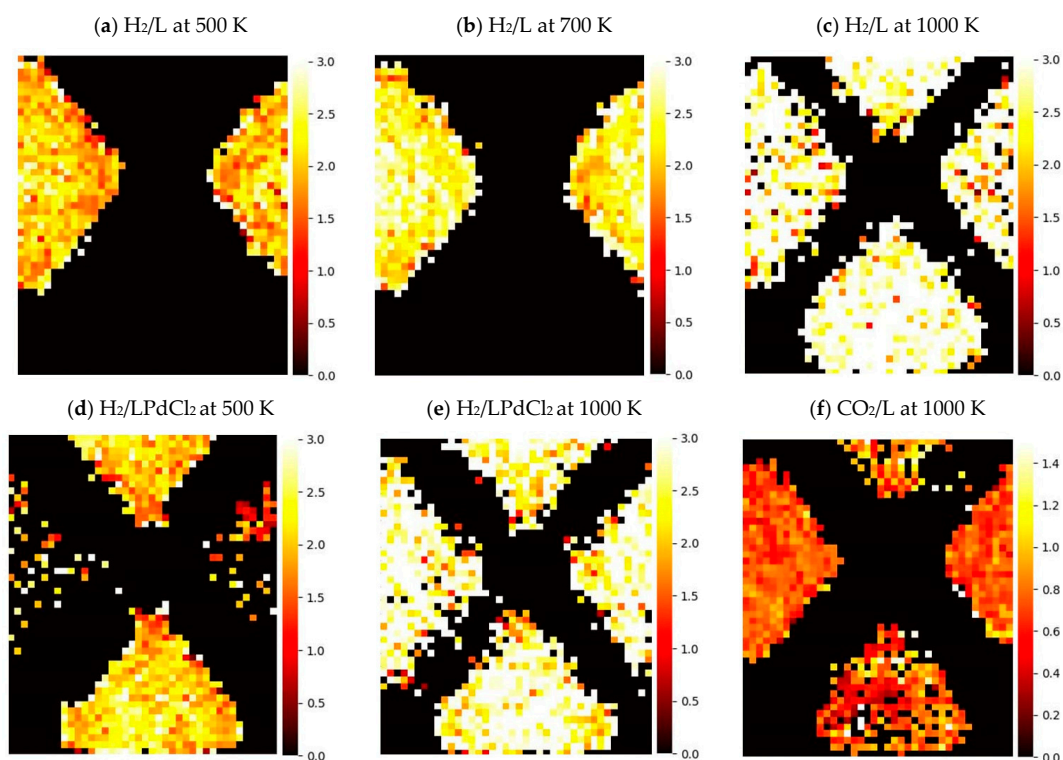


Figure 2. The heat maps of the average speed projected on an *ac*-plane of MOF-253: (a–c) 1 H₂ in L at 500, 700, and 1000 K, respectively; (d,e) 1 H₂ in LPdCl₂ at 500 and 1000 K, respectively; (f) 1 CO₂ in L

at 1000 K. Each color pixel of the heat map denotes the recorded molecular speed observed in the volume $0.5 \times b\text{-axis} \times 0.5 \text{ (\AA}^3\text{)}$ and weighted by the number of observed events. The unit of y -axis denotes the average speed at $\text{\AA}/100 \text{ fs}$. Figure S1 provides the schematic perspective of the ac -plane of MOF-253.

2.3. The Examination of the PXRD Simulation

In order to understand the relative energetics of the orientations of the linkers in MOF-253, we conducted DFT simulations to take into account the possible minimum structures using the current supercell model and identified five stable geometries as listed in Figure 3. The lowest energy orientation is found to be the trans-unidirectional orientation, being substantially lower in energy at 35.7 kcal/mol than its cis-unidirectional counterpart. The cis-unidirectional orientation is believed to be more favorable for the multi-dentate metal chelation, and also was reported in the previous post-synthesized experimental modification [13]. Both of the low-energy geometries (trans-unidirectional and trans-bidirectional) could not provide multi-dentate binding sites for post-synthesis metal chelation, where the least-stable cis-bidirectional case (66.4 kcal/mol higher than the lowest-energy orientation) may provide a tetra-dentate binding site if the metal moiety is large enough to form the inter-linker coordination bonds.

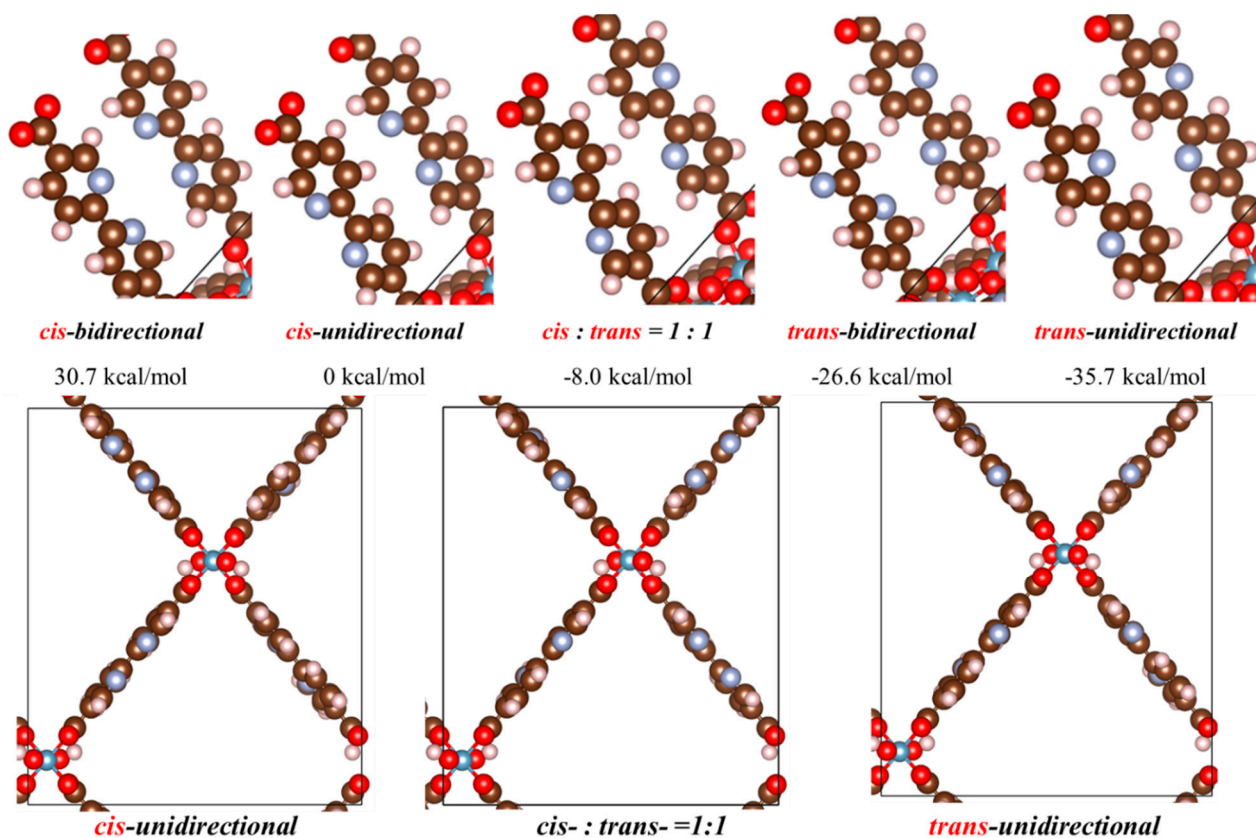


Figure 3. The schematics of linkers and the relative DFT-optimized energy to the cis-unidirectional in kcal/mol of MOF-253 isomers. Side views of the optimized structures shown below. The brown, red, pink, and indigo denote carbon, oxygen, hydrogen, and nitrogen atoms, respectively.

Figure 4a summarizes the calculated PXRD spectrum using these five optimized DFT structures, i.e., the hypothetical pristine $1 \times 1 \times 1$ supercells using VESTA [27]. All of these five linker orientations appear to have visually identical PXRD patterns so that the presence of diverse linker orientations may not be experimentally distinguishable by the spectroscopic feature of PXRD. However, it should be noted that the cis-unidirectional* model takes into account the linker distortion effect that resulted from the MCl_2 chelation, and the consequent PXRD spectrum is calculated upon the vertical removal of the

MCl_2 fragment while maintaining linker distortion. Such a comparison between the cis-unidirectional and cis-unidirectional* cases only give a trivially deviated intensity of a 2θ angle at around 12 and 17 degrees, and consequently reinforces the issue of identifying linker distortion using PXRD spectra. Figure 4b summarizes the models by considering the various percentages of MCl_2 chelation in which the current supercell can maximumly accommodate eight MCl_2 bindings. Substantial spectroscopic features are observed at the small-angle region (<10 degree) as well as some notable features between 13 and 17 degrees based upon the comparison between simulated MCl_2 -chelated and non-chelation models. Such a theoretical observation is consistent with the PXRD spectrum of as-synthesized MOF-253 [13], particularly for the <10 degree region. However, the observed spectroscopic feature between 13 and 17 degrees could either have resulted from the cases of MCl_2 chelation or non-chelation, consequently re-emphasizing the importance of the determination of the small-angle feature at <10 degree.

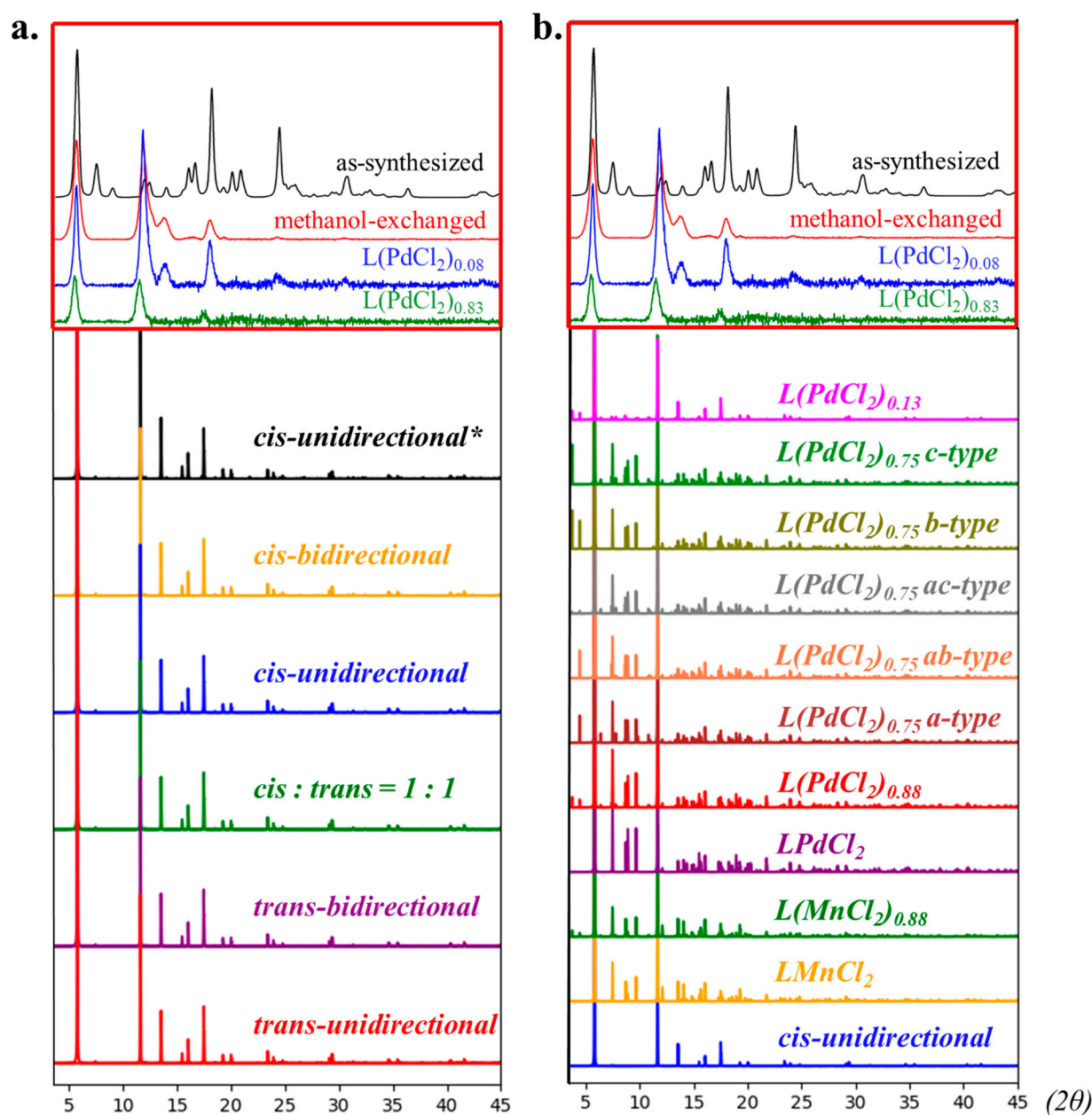


Figure 4. The simulated PXRD spectra. The red squares in (a,b) are experimental PXRD spectra that were retrieved from the report by Bloch et al. [13]. (a) The comparison between different isomers of L.

The black line with the label * is the L model that was built from L(PdCl₂) and then had the metal complexes “vertically” removed. It converted to the PXRD data without re-optimization by DFT computation. (b) The comparison between different numbers of MCl₂ incorporated into the *cis*-NN structures that were discussed in our previous study [21].

2.4. The Catalytic Mechanism for Another LPdCl₂ Isomer

We reported the theoretical analysis for the formic acid generation from CO₂ and H₂ by metal–chloro chelation in MOF-253 materials, in which PdCl₂ chelation was computationally recognized as one of the accessible catalytic candidates for the aforementioned CO₂RR catalysis [21]. The interplay between the neighboring PdCl₂ chelation moieties is investigated in this study, and several interacting PdCl₂ models from the steric hindrance perspective are theoretically optimized, as schematically shown in Figure S8. The *cis*-bidirectional structure (see Figure S8c) is identified to be marginally higher in energy than the lowest-energy *cis*-unidirectional case (see Figure S8a) by 3.14 kcal/mol. This minimal energetic difference indeed suggests that the *cis*-bidirectional orientation could be highly populated during the post-synthesis modification process. Additionally, the Pd–Pd distance of the *cis*-bidirectional model is calculated as 3.362 Å, which may facilitate the reductive elimination of two chloro-ligands to form a dimeric Pd₂Cl₂ moiety, as schematically depicted in Figure 5. The corresponding reaction energy for *cis*-bidirectional 2 × PdCl₂@MOF-253 to Pd₂Cl₂@MOF-253 + Cl₂(g) is predicted to be 72.55 kcal/mol endothermically, which could be accessible at elevated temperature conditions and is favorable by the entropic effect. The resultant binuclear Pd(I) moiety could convert CO₂ and H₂ to formic acid as schematically shown in Figure 5.

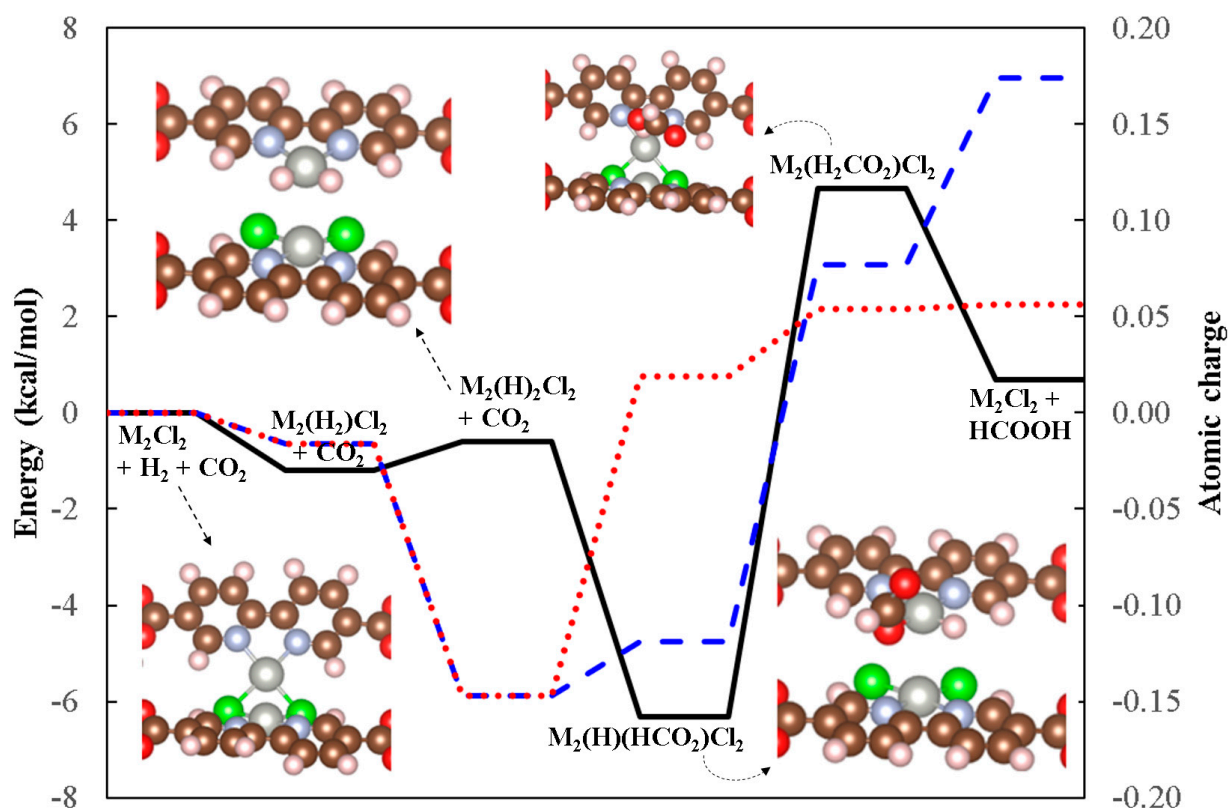


Figure 5. The energetic profile (black line) and atomic charge of hydrogen along the formic-acid-generation reaction coordinate on Pd₂Cl₂ catalytic site. The red dotted and blue dashed lines denote the calculated Hershfeld atomic charges of H bound to O and C, respectively.

Hydrogen can be exothermically adsorbed on this binuclear site with the adsorption energy at -1.91 kcal/mol, followed by inter-hydrogen bond breaking to form a PdCl₂(H)₂Pd

moiety with a minimally endothermic reaction energy at +0.58 kcal/mol. The incoming CO₂ can easily access the hydrido-ligand to form *OCHO intermediate through gaseous molecule diffusion, which can eventually result in the formation of formic acid with the predicted barrier at less than 11 kcal/mol. The desorption energy of formic acid is estimated to be only 3.97 kcal/mol exothermically due to the bidentate character of HCOOH coordination elongating the metal–chloro bridge bond. The desorption of HCOOH can finally restore the binuclear site back to its acting catalytic condition as the Pd₂Cl₂ moiety. The proposed binuclear catalytic site shows highly accessible energetics for converting CO₂ and H₂ to formic acid. A similar binuclear framework chelated in MOF-253-like materials has recently been synthesized by Wang et al. for C–H bond activation applications [28].

3. Methodology

The MOF-253 materials were described by the periodic boundary condition model using the orthorhombic unit cell ($a = 23.59 \text{ \AA}$, $b = 6.91 \text{ \AA}$, $c = 19.84 \text{ \AA}$) where the lattice constants remained frozen in the calculations. The atomic coordinates within the supercell were fully optimized, adapting the same supercell construction procedure [21], using density functional theory (DFT) or force field (FF) levels of theory. All calculations were carried out with the Amsterdam Modeling Suite (AMS) program [29,30]. There were various types of supercells used in this study, i.e., L denoting the $1 \times 1 \times 1$ bare MOF-253 unit cell without metal chelation and LPdCl₂ denoting eight units of PdCl₂ coordinated in L. Additionally, L₆ denoted six replicas along the b -axis as the $1 \times 6 \times 1$ supercell, and (LPdCl₂)₆ denoted the corresponding case containing 48 PdCl₂ chelation moieties.

UFF4MOF was adopted for the FF calculations [31], i.e., the parameter set derived from UFF [32] but extended to MOFs and TM complexes. Notably, the development of UFF4MOF was calibrated for MIL-53 materials, in which it contains the same SBUs as MOF-253. FF-MD simulations were carried out for understanding the guest molecule distribution at the finite temperature conditions (300–1000 Kelvin) under the NVT ensemble with the Berendsen thermostat. The integration timestep of FF-MD was chosen at 0.5 fs. The cutoff of the non-bonding interaction was chosen at 15 Å while particle smash Ewald summation was used for the Coulomb interaction. Despite the decomposition of MOF-253 at 700 K and the metal coordinated case at 650 K [13] observed via the experimental thermal gravimetric analysis, the temperature of the current MD simulations still exceeded beyond 700 K during the exploration of the dynamic phenomena of linker movements. As explained in the above Results and Discussion Section, the linker rotation barrier is substantially overestimated at FF level than the predicted barrier at DFT. Conducting FF-MD simulations at temperatures higher than 700 K can still provide the chemical significance for understanding the atomistic dynamics at a highly mobile condition while maintaining reasonable computational costs. The FF-MD simulations were pre-equilibrated for 0.5 ns, followed by the production run for another 0.5 ns with snapshots recorded every 100 fs.

DFT simulations were conducted with the generalized gradient approximation (GGA) with the Perdew–Burke–Ernzerh (PBE) exchange–correlation functional [33] with all of the atoms described by a triple-zeta-quality atom-centered basis set with one polarization function. For the inclusion of van der Waals interactions, the D3 version of Grimme’s dispersion Becke–Johnson damping [34,35] was applied. Moreover, the scalar relativity effect was treated by the zero-order regular approximation (ZORA) approach [36]. The convergence criteria were set as 10^{-5} eV for total energy change and 0.01 Å for a total Cartesian step change. The DFT calculation was carried out by the BAND module of AMS. Additionally, the PXRD pattern was simulated by the Powder Diffraction Pattern utility in VESTA software.

4. Conclusions

In this study, we present a series of classical molecular dynamics simulations for understanding the linker dynamic effect on the guest molecule adsorption in MOF-253 materials. All of the possible linker orientations were explored and subsequently optimized

by DFT calculation, and the simulated PXRD patterns were investigated. The motion of bpydc rotation was found to facilitate the guest molecule penetrating various pores in MOF-253, and the steric hindrance introduced by TM chelation can even benefit the linker rotation. The corresponding simulated PXRD patterns of these non-TM-chelated structures indicate the challenges of identifying distinguishable spectroscopic features for classifying linker orientations. The spectroscopic features at 2θ angle less than 10 degrees appear to suggest the presence of TM chelation. Interestingly, a PdCl₂-chelated minimum structure, labeled as *cis*-bidirectional orientation, contains the short Pd-Pd distance that can result in the formation of a binuclear Pd₂Cl₂ catalytic site. Such a binuclear reaction center was found to substantially favor the formic acid generation mechanism from CO₂ + H₂ with the predicted catalytic barrier at less than 11 kcal/mol based upon the DFT calculation results.

Supplementary Materials: The following supporting information can be downloaded at: <https://www.mdpi.com/article/10.3390/molecules29133211/s1>, Figure S1: The schematic representation of the MOD-253 model; Figures S2–S4: Linker rotation dynamics; Figures S5–S7: Heat maps of MD simulation with guest molecule adsorption; Figure S8: Schematic representation of TM chelation and the energetics; Tables S1–S3: Statistics of the structure dynamics of MD simulations; Table S4: Guest molecule structure comparison; Tables S5–S9: Statistics of MD simulation with gas adsorption.

Author Contributions: Methodology and data curation: M.-C.H. and W.-L.L. Draft writing—review and editing: M.-C.H., C.-C.C. and M.-K.T. Conceptualization and supervision: C.-C.C. and M.-K.T. All authors have read and agreed to the published version of the manuscript.

Funding: This study is supported by the National Science and Technology Council of Taiwan (112-2113-M-034-002-MY3 and 112-2113-M-003-019).

Institutional Review Board Statement: Not applicable.

Informed Consent Statement: Not applicable.

Data Availability Statement: The data are contained within the article.

Acknowledgments: The authors are grateful for the computational resources provided by the National Center for High-Performance Computing of Taiwan and the Center for Cloud Computing in National Taiwan Normal University.

Conflicts of Interest: The authors declare no conflicts of interest.

References

1. Forgan, R.S. Modulated self-assembly of metal-organic frameworks. *Chem. Sci.* **2020**, *11*, 4546–4562. [[CrossRef](#)] [[PubMed](#)]
2. Shakya, D.M.; Ejegbavwo, O.A.; Rajeshkumar, T.; Senanayake, S.D.; Brandt, A.J.; Farzandh, S.; Acharya, N.; Ebrahim, A.M.; Frenkel, A.I.; Rui, N.; et al. Selective Catalytic Chemistry at Rhodium(II) Nodes in Bimetallic Metal–Organic Frameworks. *Angew. Chem. Int. Ed.* **2019**, *58*, 16533–16537. [[CrossRef](#)] [[PubMed](#)]
3. Szécsényi, Á.; Li, G.; Gascon, J.; Pidko, E.A. Unraveling reaction networks behind the catalytic oxidation of methane with H₂O₂ over a mixed-metal MIL-53(Al,Fe) MOF catalyst. *Chem. Sci.* **2018**, *9*, 6765–6773. [[CrossRef](#)] [[PubMed](#)]
4. Zhang, Y.; Yang, X.; Zhou, H.-C. Synthesis of MOFs for heterogeneous catalysis via linker design. *Polyhedron* **2018**, *154*, 189–201. [[CrossRef](#)]
5. Yang, Q.; Xu, Q.; Jiang, H.-L. Metal–organic frameworks meet metal nanoparticles: Synergistic effect for enhanced catalysis. *Chem. Soc. Rev.* **2017**, *46*, 4774–4808. [[CrossRef](#)] [[PubMed](#)]
6. Gao, F.; Yan, R.; Shu, Y.; Cao, Q.; Zhang, L. Strategies for the application of metal–organic frameworks in catalytic reactions. *RSC Adv.* **2022**, *12*, 10114–10125. [[CrossRef](#)] [[PubMed](#)]
7. Luo, Y.-H.; Dong, L.-Z.; Liu, J.; Li, S.-L.; Lan, Y.-Q. From molecular metal complex to metal-organic framework: The CO₂ reduction photocatalysts with clear and tunable structure. *Coord. Chem. Rev.* **2019**, *390*, 86–126. [[CrossRef](#)]
8. Seo, J.S.; Whang, D.; Lee, H.; Jun, S.I.; Oh, J.; Jeon, Y.J.; Kim, K. A homochiral metal–organic porous material for enantioselective separation and catalysis. *Nature* **2000**, *404*, 982–986. [[CrossRef](#)] [[PubMed](#)]
9. Kent, C.A.; Mehl, B.P.; Ma, L.; Papanikolas, J.M.; Meyer, T.J.; Lin, W. Energy Transfer Dynamics in Metal–Organic Frameworks. *J. Am. Chem. Soc.* **2010**, *132*, 12767–12769. [[CrossRef](#)]
10. Wang, C.; Xie, Z.; deKrafft, K.E.; Lin, W. Doping Metal–Organic Frameworks for Water Oxidation, Carbon Dioxide Reduction, and Organic Photocatalysis. *J. Am. Chem. Soc.* **2011**, *133*, 13445–13454. [[CrossRef](#)]
11. Chen, F.; Drake, H.F.; Feng, L.; Powell, J.A.; Wang, K.-Y.; Yan, T.-H.; Zhou, H.-C. Metal–Organic Frameworks as Versatile Platforms for Organometallic Chemistry. *Inorganics* **2021**, *9*, 27. [[CrossRef](#)]

12. Kaes, C.; Katz, A.; Hosseini, M.W. Bipyridine: The Most Widely Used Ligand. A Review of Molecules Comprising at Least Two 2,2'-Bipyridine Units. *Chem. Rev.* **2000**, *100*, 3553–3590. [[CrossRef](#)] [[PubMed](#)]
13. Bloch, E.D.; Britt, D.; Lee, C.; Doonan, C.J.; Uribe-Romo, F.J.; Furukawa, H.; Long, J.R.; Yaghi, O.M. Metal Insertion in a Microporous Metal–Organic Framework Lined with 2,2'-Bipyridine. *J. Am. Chem. Soc.* **2010**, *132*, 14382–14384. [[CrossRef](#)] [[PubMed](#)]
14. Fei, H.; Cohen, S.M. A robust, catalytic metal–organic framework with open 2,2'-bipyridine sites. *Chem. Commun.* **2014**, *50*, 4810–4812. [[CrossRef](#)] [[PubMed](#)]
15. Liu, H.; Peng, X.; Zeng, H. Synthesis, structure and luminescence property of Eu(III) metal–organic framework based on 2,2'-bipyridine-5,5'-dicarboxylic acid. *Inorg. Chem. Commun.* **2014**, *46*, 39–42. [[CrossRef](#)]
16. Vizuet, J.P.; Lewis, A.L.; McCandless, G.T.; Balkus, K.J. Synthesis and characterization of a holmium 2,2'-bipyridine-5,5'-dicarboxylate MOF: Towards the construction of a suitable holmium carrier. *Polyhedron* **2019**, *159*, 12–17. [[CrossRef](#)]
17. Wu, Y.; Wei, L.; Wang, H.; Chen, L.; Zhang, Q. First principles study of enhanced CO₂ adsorption on MOF-253 by salt-insertion. *Comput. Mater. Sci.* **2016**, *111*, 79–85. [[CrossRef](#)]
18. Deng, X.; Qin, Y.; Hao, M.; Li, Z. MOF-253-Supported Ru Complex for Photocatalytic CO₂ Reduction by Coupling with Semidehydrogenation of 1,2,3,4-Tetrahydroisoquinoline (THIQ). *Inorg. Chem.* **2019**, *58*, 16574–16580. [[CrossRef](#)] [[PubMed](#)]
19. Sun, D.; Gao, Y.; Fu, J.; Zeng, X.; Chen, Z.; Li, Z. Construction of a supported Ru complex on bifunctional MOF-253 for photocatalytic CO₂ reduction under visible light. *Chem. Commun.* **2015**, *51*, 2645–2648. [[CrossRef](#)] [[PubMed](#)]
20. Wang, N.; Xie, J.; Zhang, J. MOF-253 immobilized Pd and Cu as recyclable and efficient green catalysts for Sonogashira reaction. *Arab. J. Chem.* **2022**, *15*, 103962. [[CrossRef](#)]
21. Hsieh, M.-C.; Krishnan, R.; Tsai, M.-K. Formic Acid Generation from CO₂ Reduction by MOF-253 Coordinated Transition Metal Complexes: A Computational Chemistry Perspective. *Catalysts* **2022**, *12*, 890. [[CrossRef](#)]
22. Gonzalez-Nelson, A.; Coudert, F.-X.; van der Veen, M.A. Rotational Dynamics of Linkers in Metal–Organic Frameworks. *Nanomaterials* **2019**, *9*, 330. [[CrossRef](#)] [[PubMed](#)]
23. Gould, S.L.; Tranchemontagne, D.; Yaghi, O.M.; Garcia-Garibay, M.A. Amphidynamic Character of Crystalline MOF-5: Rotational Dynamics of Terephthalate Phenylenes in a Free-Volume, Sterically Unhindered Environment. *J. Am. Chem. Soc.* **2008**, *130*, 3246–3247. [[CrossRef](#)] [[PubMed](#)]
24. Yan, Y.; Kolokolov, D.I.; da Silva, I.; Stepanov, A.G.; Blake, A.J.; Dailly, A.; Manuel, P.; Tang, C.C.; Yang, S.; Schröder, M. Porous Metal–Organic Polyhedral Frameworks with Optimal Molecular Dynamics and Pore Geometry for Methane Storage. *J. Am. Chem. Soc.* **2017**, *139*, 13349–13360. [[CrossRef](#)] [[PubMed](#)]
25. Inukai, M.; Fukushima, T.; Hijikata, Y.; Ogiwara, N.; Horike, S.; Kitagawa, S. Control of Molecular Rotor Rotational Frequencies in Porous Coordination Polymers Using a Solid-Solution Approach. *J. Am. Chem. Soc.* **2015**, *137*, 12183–12186. [[CrossRef](#)] [[PubMed](#)]
26. Vogelsberg, C.S.; Uribe-Romo, F.J.; Lipton, A.S.; Yang, S.; Houk, K.N.; Brown, S.; Garcia-Garibay, M.A. Ultrafast rotation in an amphidynamic crystalline metal organic framework. *Proc. Nat. Acad. Sci. USA* **2017**, *114*, 13613–13618. [[CrossRef](#)] [[PubMed](#)]
27. Momma, K.; Izumi, F. VESTA: A three-dimensional visualization system for electronic and structural analysis. *J. Appl. Crystallogr.* **2008**, *41*, 653–658. [[CrossRef](#)]
28. Wang, Z.; Yeary, P.; Feng, X.; Lin, W. Self-adaptive Metal–Organic Framework Assembles Di-iron Active Sites to Mimic Monooxygenases. *J. Am. Chem. Soc.* **2023**; ahead of print. [[CrossRef](#)] [[PubMed](#)]
29. te Velde, G.; Bickelhaupt, F.M.; Baerends, E.J.; Fonseca Guerra, C.; van Gisbergen, S.J.A.; Snijders, J.G.; Ziegler, T. Chemistry with ADF. *J. Comput. Chem.* **2001**, *22*, 931–967. [[CrossRef](#)]
30. Rüger, R.; Franchini, M.; Trnka, T.; Yakovlev, A.; Lenthe, E.v.; Philipsen, P.; Vuren, T.v.; Klumpers, B.; Soini, T. *Amsterdam Modeling Suite*, AMS2020.101; SCM: Amsterdam, The Netherlands, 2020.
31. Coupry, D.E.; Addicoat, M.A.; Heine, T. Extension of the Universal Force Field for Metal–Organic Frameworks. *J. Chem. Theory Comput.* **2016**, *12*, 5215–5225. [[CrossRef](#)] [[PubMed](#)]
32. Rappe, A.K.; Casewit, C.J.; Colwell, K.S.; Goddard, W.A., III; Skiff, W.M. UFF, a full periodic table force field for molecular mechanics and molecular dynamics simulations. *J. Am. Chem. Soc.* **1992**, *114*, 10024–10035. [[CrossRef](#)]
33. Perdew, J.P.; Burke, K.; Ernzerhof, M. Generalized Gradient Approximation Made Simple. *Phys. Rev. Lett.* **1996**, *77*, 3865–3868. [[CrossRef](#)] [[PubMed](#)]
34. Grimme, S.; Antony, J.; Ehrlich, S.; Krieg, H. A consistent and accurate ab initio parametrization of density functional dispersion correction (DFT-D) for the 94 elements H–Pu. *J. Chem. Phys.* **2010**, *132*, 154104. [[CrossRef](#)] [[PubMed](#)]
35. Grimme, S.; Ehrlich, S.; Goerigk, L. Effect of the damping function in dispersion corrected density functional theory. *J. Comput. Chem.* **2011**, *32*, 1456–1465. [[CrossRef](#)]
36. Lenthe, E.v.; Snijders, J.G.; Baerends, E.J. The zero-order regular approximation for relativistic effects: The effect of spin–orbit coupling in closed shell molecules. *J. Chem. Phys.* **1996**, *105*, 6505–6516. [[CrossRef](#)]

Disclaimer/Publisher’s Note: The statements, opinions and data contained in all publications are solely those of the individual author(s) and contributor(s) and not of MDPI and/or the editor(s). MDPI and/or the editor(s) disclaim responsibility for any injury to people or property resulting from any ideas, methods, instructions or products referred to in the content.